

Supplementary information for article "Revealing polymerization kinetics with colloidal dipatch particles"

Simon Stuij *et al.*

PATCHY PARTICLE DETAILS

Synthesis

The colloidal di-patch and tetra-patch particles were prepared by a recently published colloidal fusion protocol [1]. In accordance with the protocol, the synthesis was done following four main steps. (i) First, monodisperse, negatively charged, solid spheres of PS with a diameter of approximately $2.2 \mu\text{m}$ were synthesized. The spheres are prepared by dispersion polymerization with Potassium persulfate (KPS) as radical initiator and Polyvinylpyrrolidone (PVP). These spheres were measured to be negatively charged in water with a zeta potential $V_{zeta} = -55(5) \text{ mV}$ at 12.5mM NaCl . Using these spheres we deviate slightly from the published protocol which uses purely sterically PVP stabilized PS, or positively charged PS spheres. This was done because sterically stabilized PS are less charged, and therefore less convenient for critical Casimir assembly which requires a hydrophilic PS matrix. The positively charged PS particles were also explored but turned out to be unstable in the binary mixture. In addition, we synthesized two batches of monodisperse TPM oil droplets with approximate sizes of 1 and $0.65 \mu\text{m}$ that were used for the tetra and dipatch particles, respectively. The TPM oil was fluorescently dyed with rhodamine. (ii) Next, liquid colloidal clusters were created by mixing the solid sphere and oil droplets. In the case of the tetrapatch particles four spheres assembled around a single liquid core. Because of the chosen size ratio between PS spheres and TPM droplets of $\alpha \approx 2$, this resulted in close-packed tetrahedrons with a liquid TPM core. In the case of the dipatch particles ($\alpha \approx 3$), that three solid spheres assemble around a liquid core (iii) Next, 5%wt. dodecyltrimethylammonium bromide (DTAB) is added to the cluster suspension to reach a final concentration of 0.8%wt, followed by the addition of a PS plasticizer (tetrahydrofuran) which caused the PS spheres to deform and effectively fuse, while extruding the liquid TPM core through the interstices of the cluster. The addition of DTAB is necessary because it changes the interfacial tension of PS/TPM making the extrusion more favorable. In addition some F108 stabilizing surfactant was added to the suspension before THF, to further stabilize the clusters. This resulted in a spherical tetrapatch or dipatch particle with liquid TPM patches. (iv) Finally, the TPM patches are solidified through polymerization, using AIBN as radical initiator. The resulting patchy

particles are charge stabilized in water, though for long time storage extra F108 stabilizing surfactant was used.

Patch size characterization

After synthesis, the morphology of the patchy particles was carefully characterized. The particles have an average diameter of $d = 3.2(1) \mu\text{m}$, and $d = 3.7(1) \mu\text{m}$ for dipatch and tetrapatch particles respectively, where the uncertainty is the polydispersity. These sizes were determined in the same solution in which assembly experiments were performed to take possible swelling effects into account. To measure their sizes, we assembled the particles patch to patch and measured the center-to-center distance between touching particles using optical microscopy. As a consistency check we note that the ratio of dipatch to tetrapatch size is $1.15(\pm 0.05)$. This is close to the expected ratio $(4/3)^{1/3} \approx 1.1$, which is derived from the fact that dipatch particles are made from three PS spheres and tetrapatch particles from four PS spheres.

In addition, we determined the average patch size of each particle type using a setup that combines optical and atomic force microscopy (AFM). Samples were dried on glass slides such that monolayers form at the drying front. After locating a patch in the right orientation a surface scan was performed, which revealed spherical patches, see Fig. 1. The edge of the patch is clearly recognized by a narrow trench and a change in curvature marking the transition from PS bulk to TPM patch material. This trench is caused by the wetting difference between PS and TPM, and reveals the nonzero contact angle between PS and TPM at the material transition point. We determined the size of the patch by measuring the projected patch diameter d_p as defined in Fig. 1(a,b). This was done by drawing linear profiles crossing the center of the patch and measuring the distance between the patch-bulk transition points. These linear profiles in addition showed a good fit with a sphere with diameter $d = 3.5 \pm 0.1 \mu\text{m}$ for the tetrapatch particles and $d = 3.3 \pm 0.1 \mu\text{m}$ in the case of dipatch particles, Fig. 1(red dotted lines). This value is in approximate agreement with the particle radii in solution validating the AFM measurements, minor differences are to be expected from the fact that particles are dried before AFM measurement.

We quantified the patch size in terms of the patch arc angle θ_p , which is a particle size independent measure-

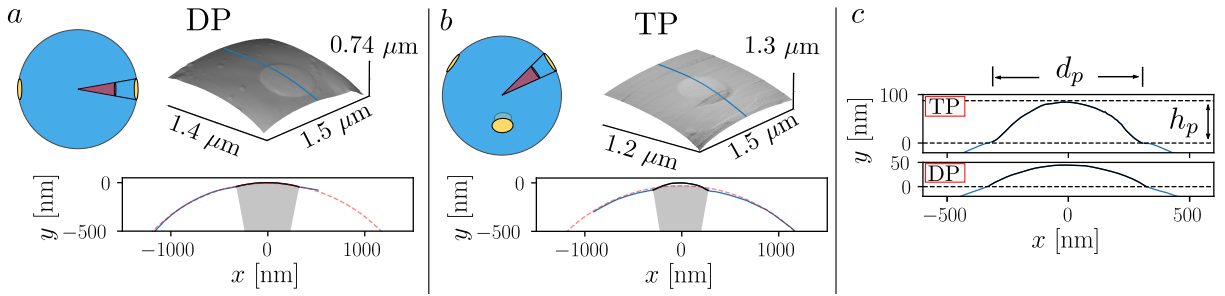


FIG. 1. **AFM measurements of the particle patches.** (a) Dipatch particles: Schematic indicating definition of projected patch diameter d_p and patch arc angle θ_p , surface height measured using AFM (zoom on patch) and height profile along the blue line indicated in the surface plot. (b) Tetrapatch particle (c) Height profile zoomed in on patch, aspect ratio between x and y is set to 2.

Particle type	d [μm]	d_p [μm]	θ_p [$^\circ$]	h_p [nm]	R_p [μm]	σ_p [%]
Dipatch	3.2(1)	0.58(5)	21(2)	45(5)	1.0(2)	1.6(2)
Tetrapatch	3.7(1)	0.54(5)	17(2)	84(5)	0.5(1)	2.4(5)

TABLE I. Patchy particle patch morphology parameters measured using AFM, from left to right: Particle diameter d (determined in solution using optical microscopy), projected patch diameter d_p , patch arc-angle θ_p , patch height h_p , patch radius of curvature R_p , total particle surface fraction covered by patches σ_p

ment of the patch size, see schematic Fig. 1(a,b). The patch arc angle was determined from the projected patch diameter d_p and particle diameter d using the relation $\theta_p = 2 \sin^{-1}(d_p/d)$, see table I(third column). Here, the uncertainty is the standard deviation of the measured patches and gives the patch size polydispersity. We note that the polydispersity is a rough estimation limited by the low measurement statistics.

Apart from patch sizes, the AFM measurements also provide information on the height h_p of patches. Not all patches stick out equally, as shown by the profiles that are zoomed-in on the patch Fig. 1(c). This results in a different curvature at the patch than for the rest of the particle. Modelling the patches as spherical caps, we can extract the radius of curvature R of each patch via $R = ((d_p/2)^2 + h_p^2) / 2h_p$, see table I. Next to patch size, the patch curvature will influence the inter-patch interaction, as a higher curvature results in less contact when patches are close together and is therefore expected to decrease the interaction strength. In addition we determined the area of each patch using the relation for spherical caps $A = \pi ((d_p/2)^2 + h_p^2)$. The total fraction of the particle surface that is covered with patch material σ_p is then $\sigma_p = 4A/(\pi d^2)$ for tetrapatch particles and $\sigma_p = 2A/(\pi d^2)$ for dipatch particles, see table I.

PATCHY CRITICAL CASIMIR SIMULATION DETAILS

Binary mixture phase diagram

To determine the critical Casimir interaction potential, knowledge of the binary mixture is required, as this determines the correlation length of the near-critical solvent fluctuations. In the experiments, the control parameters are the concentration c and the temperature difference to the phase separation temperature $\Delta T_{cx} = T_{cx} - T$. The concentration c is kept fixed at $c = 25\%vol$ lutidine. The phase separation temperature T_{cx} is determined by performing a slow temperature ramp and noting the set temperature at which phase separation occurs. By subtracting this with T we eliminate the influence of possible calibration errors in the thermal probe.

To determine the critical Casimir interaction, knowledge of $\Delta T = T_c - T$ is required. To transform ΔT_{cx} to ΔT we use the relation $\frac{T_{cx} - T_c}{T_c} = \left(\frac{|c_c - c|}{B}\right)^{1/\beta}$. Here $\beta = 0.325$ is a universal scaling constant, and B is a non-universal constant that depends on the binary mixture, and c is measured in percent by weight. We use $B = 0.765$ [1/%wt] for lutidine water, obtained from ref. [2], and $c_c = 28.7$ percent by weight and $T_c = 33.86^\circ\text{C}$, obtained from ref. [3]. The phase diagram of lutidine water using these parameters is shown in Fig. 2(a). Here lutidine concentration is converted from weight percent to volume percent. The temperatures, at which the equilibrium measurements of the main text have been performed are indicated by black squares.

Simulation potentials

The patchy particle potentials that are used for the simulation are shown for various temperatures in Fig. 2(b). The switching function, which takes into account the finite patchsize, is shown in Fig. 2(c). These potentials are based on the physical dimensions of the

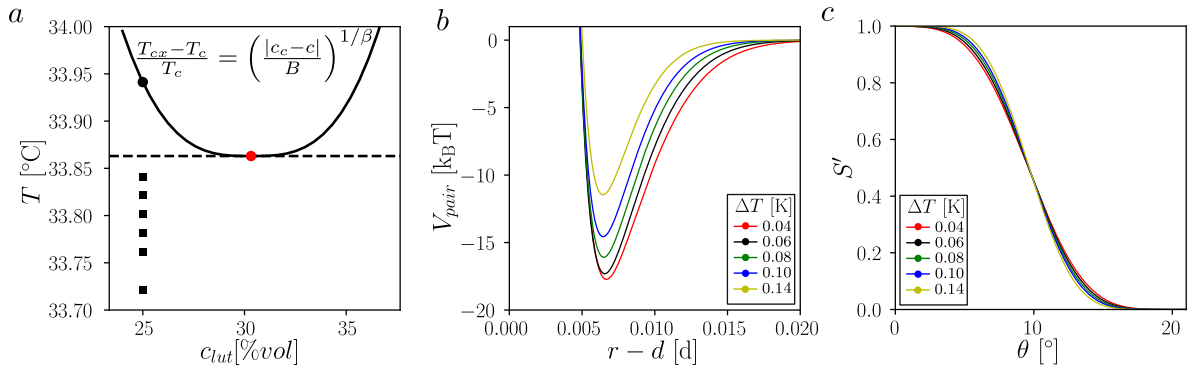


FIG. 2. **Solvent phase diagram and critical Casimir interactions.** (a) Phase diagram of the binary lutidine-water mixture with indicated critical point (red dot) and state points, at which the experiments in the manuscript have been performed (black squares). (b) Pair potentials used for simulations between the spherical particle patches directly facing each other, i.e. $S_{p_k, p_l}(\Omega_i, \Omega_j) = 1$, as a function of temperature (c) Switching functions as a function of the relative orientation of the patches.

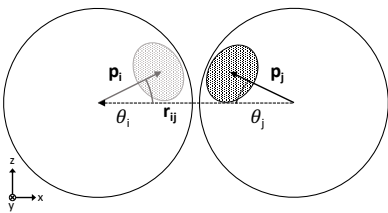


FIG. 3. **schematic illustration of two patchy particles.** The interparticle vector r_{ij} and the patch vector \vec{p} are indicated. The angle θ_x is calculated via $\cos \theta_x = (\vec{p}_x \cdot r_{ij} / |\vec{p}_x| |r_{ij}|)$ with $x = i$ or j . Illustration from Ref. [4].

dipatch patchy particle in Table I and solvent conditions described above. In addition, three parameters are benchmarked onto the chain length distribution and bending rigidity measurements. The benchmarking procedure is described in a separate publication [4]. For completeness we here report the final potentials and parameters.

The total potential, given by Eq. 1, consists of pair potentials acting between the particles with n_p patches, inter particle distance $r_{ij} = |\vec{r}_i - \vec{r}_j|$ and orientations Ω_i and Ω_j in the quaternion representation, and a gravitational potential acting on each particle as a function of the vertical component of the position \vec{r} to mimic the sedimentation of the particles to the bottom of the capillary.

The external potential $V_{gravity}$, given in Eq. 2, consists of two parts: a linear part with a slope equal to the gravitational force F_g , and an additional Lennard Jones (LJ) 12-6 potential mimicking the capillary wall interaction. At the boundary z_b , the values and first derivatives of both expressions are equal to order $\mathcal{O}(1e-04) k_B T$. We used $\epsilon_{LJ} = 500 k_B T$ and calculated $F_g \approx -7.70 k_B T/d$ based on the density difference between the solvent and dipatch particle, $b \approx 8.64d$ and $z_d \approx 1.12d$.

The pair potential V_{pair} , given by Eq. 3, is based on

the work in Ref [5]. This potential contains a screened electrostatic repulsion V_{rep} and an attractive interaction between two patches p_k and p_l in V_{p_k, p_l} . As only one pair of patches is able to form a bond, the patch pair with the minimum interaction energy is counted. The attractive term is a temperature-dependent critical Casimir attraction V_C which is only effective if the patches are aligned via the switching function S , given by Eq. 4. The electrostatic repulsion depends on the Debye length $\kappa^{-1} = 2.78$ nm obtained from the experimental solvent and added salt. In addition it depends on the surface charge σ_q , which is used as the first benchmark parameter. We obtain an optimized value $\sigma_q = 0.09 e/nm^2$. The critical Casimir potential depends on the correlation length ξ of the binary mixture which is obtained from the experimental solvent parameters. In addition it depends on a material specific parameter w that captures the hydrophilic or -phobic affinity of the patch material with the solvent. This parameter is used as a second benchmark parameter [2]. We obtain an optimized value $w = 0.462$.

The function S_{p_k, p_l} acts as a switching function to capture the effective critical Casimir interaction depending on the relative orientation of the patches. It is approximated by $S_{p_k, p_l}(\Omega_i, \Omega_j) \approx S'(\theta_i) S'(\theta_j)$ in which θ is the angle between the inter particle vector r_{ij} and the patch vectors \vec{p} , the vector pointing from the center of the particle to the center of the patch, see Fig. 3. The function S' is constructed upon an integration of V_C and depends on the effective patch width θ_p^{eff} . This parameter is used as the third benchmarking parameter. We obtain an optimized value $\theta_p^{eff} = 19.5^\circ$, consistent with AFM measurement, see Table I.

$$V = \sum_{i>j}^N V_{pair}(r_{ij}, \Omega_i, \Omega_j) + \sum_i^N V_{gravity}(z_i) \quad (1)$$

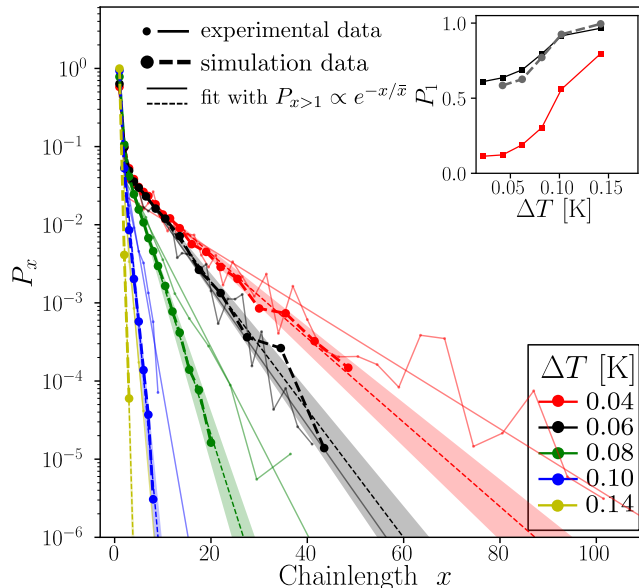


FIG. 4. **Equilibrium chain-length distributions.** Chain-length distributions of simulations (big dots) and experiments (small dots) for various temperatures at surface coverage $\phi = 0.3$, a logarithmic binning was used. Dotted lines are exponential fits to simulation data, while thin solid lines are the exponential fits to the experimental data, presented in the main text. The inset shows the experimental/simulated probability of singlets (black/grey) as a function of temperature. The red curve shows the expected singlet probability based on an exponential distribution, which is equal to $1 - p_b$, where p_b is the experimental binding probability. Simulations reproduce both the exponential decay for longer chain lengths and the surplus of singlets.

$$V_{gravity}(z) = \begin{cases} 4\epsilon_{LJ} \left(\frac{d^{12}}{z} - \frac{d^6}{z} + \frac{1}{4} \right), & z \leq z_b \\ -F_g z + b, & z > z_b \end{cases} \quad (2)$$

$$V_{pair}(r_{ij}, \Omega_i, \Omega_j) = V_{rep}(r_{ij}) + \min_{1 \leq k, l \leq n_p} V_{p_k, p_l}(r_{ij}, \Omega_i, \Omega_j) \quad (3)$$

$$V_{p_k, p_l}(r_{ij}, \Omega_i, \Omega_j) = V_C(r_{ij}) S_{p_k, p_l}(\Omega_i, \Omega_j) \quad (4)$$

Monte Carlo simulation details

For the Monte Carlo simulations, we use a rectangular box of lengths $43.6d$, $60.0d$, and $43.6d$ for the x -, y -, and z -direction, respectively, with periodic boundary conditions. The box contains 666 up to 2000 dipatch particles depending on the surface coverage ranging from 0.2 to 0.6, respectively.

The dipatch particles are randomly placed in the simulation box and equilibrated and measured for $\sim 2 \times 10^{10}$ and $\sim 1.5 \times 10^{10}$ MC steps, respectively. During each MC step, either a single particle (95%) or cluster move (5%) is performed by a rotation (50%) or a translation (50%). A cluster is defined as a structure containing particles that are connected via bonds where a bond

is identified if the attractive part of the pair potential $V_C(r_{ij})S'(\theta_i)S'(\theta_j) < 0k_B T$. The single particle is randomly selected with a $1/N_{\text{part}}$ chance, while the cluster has a $1/N_{\text{cluster}}$ chance with N_{part} the total number of particles and N_{cluster} the total number of clusters. Therefore, to ensure detailed balance, during the cluster moves no formation of bonds is allowed to keep N_{cluster} constant.

The rotation is performed by a random quaternion with a rotation angle in a uniform distribution $\in [-dq_{\text{max}}, dq_{\text{max}}]$. The single particle is rotated around its center, while the cluster is rotated around the center of a randomly selected particle in the cluster. The clusters are rotated along the z -axis to enhance sampling in the quasi-2D x, y -plane due to the presence of gravity. The translation is performed by creating a random translation vector \vec{r}_t with its x -, y -, and z -component uniformly chosen $\in [-dr_{\text{max}}, dr_{\text{max}}]$. Before the translation is being performed along \vec{r}_t , the z -component of the translation is reduced by a factor 10 to enhance sampling in the quasi-2D x, y -plane. During sampling, dq_{max} and dr_{max} of the single particle and cluster moves are adapted such that the acceptance ratio lies between 30-70%.

Simulated chain-length distributions and nematic transition

The chain-length distributions are calculated from the average of two independent samples, simulated with

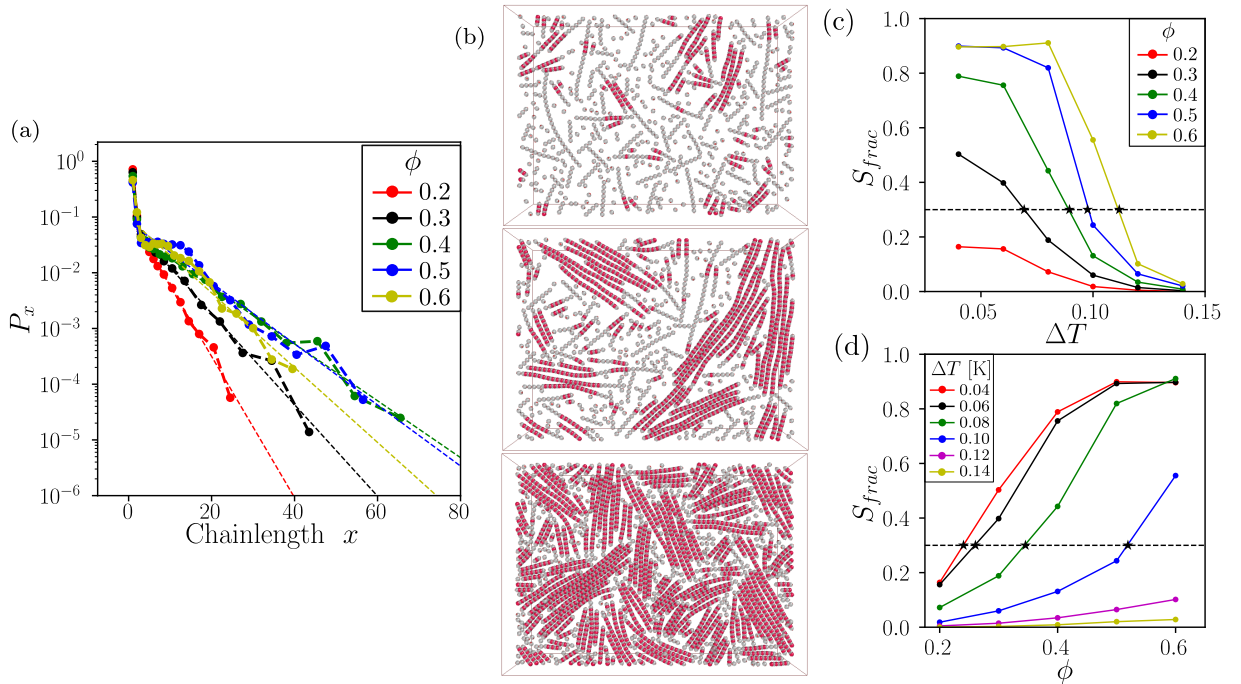


FIG. 5. **Isotropic-nematic transition in simulations.** (a) Chain length distributions of simulated chains and exponential fits for various surface coverages at fixed $\Delta T = 0.06\text{K}$. As in experiments, the trend of increasing chain length with surface coverage reverses above $\phi = 0.4$. The obtained values of \bar{x} are shown in Fig. 3(b) of the main text. (b) Snapshots of the simulations at $\Delta T = 0.06\text{K}$ and $\phi = 0.3, 0.4$ and 0.6 corresponding to the experimental snapshots of Fig. 3d in the main text. Red dots indicate locally nematic environments in which $S(i) > 0.4$. (c) Nematic ratio S_{frac} as a function of ΔT for various surface coverages. (d) The same data as in (c) but plotted as a function of ϕ . Black stars in (c) and (d) are linearly interpolated values at which $S_{frac} = 0.3$. These points are used as the demarcation line for the nematic state in Fig. 3h of the main text.

Monte Carlo at temperatures ranging from $\Delta T = 0.14\text{K}$ to 0.04K and surface coverage ranging from $\phi = 0.2$ to 0.6 . The resulting equilibrium chain length distributions at $\phi = 0.3$ are shown in Fig. 4. To obtain the characteristic length \bar{x} , exponential fits were performed, shown as dotted straight lines and shaded regions indicating the variances of the fits. We also include the experimental distributions as presented in the main manuscript for comparison (thin data points and lines). The obtained values of \bar{x} are shown, and compared with the experimental ones, in Fig. 2(d) of the main text. The inset shows the probability of singlets, P_1 , as a function of temperature for experiment (black) and simulation (grey). In addition, the expected probability of singlets for fully exponential distributions, $1 - p_b$, is shown in red. The excess of singlets with respect to an exponential distribution that is seen in experiments is reproduced by simulation.

For some temperatures, some deviations between experimental and simulated distributions are observed. In particular, the highest temperature (red curve) shows longer chains for experiments than simulation. This can be explained by the fact that at this high temperature, some non-dipatch particles that were inevitably also

present in the sample (singlets and permanent clusters) started attracting, binding with more than 2 neighbors. This resulted in the presence of a minor population of branched chains, as can also be seen in the snapshots in Fig. 2(a) of the main text, driving up chain length. In addition, temperatures lower than 0.06 show longer chains for experiments than simulation. For the lowest temperatures this is explained by the presence of some permanent non-Casimir bonded clusters in the experiment. Remaining deviations are explained by the fact that simulation parameters were benchmarked to also agree with bending rigidity measurements which resulted in an optimal compromise, which is discussed in more detail in [4].

Very similar to the experimental measurements, there is a non-monotonic trend observed in the chain length distribution as function of density that is associated with the formation of nematic regions. The effects of increasing concentration while keeping temperature fixed on the simulated system are shown in Fig. 5. Initially, the chain length increases as a function of particle density ($\phi=0.2-0.4$), but then it decreases as density is further increased ($\phi=0.5,0.6$). This non-monotonic trend is of kinetic origin, indicating that the systems at $\phi \geq 0.5$ has not reached the equilibrium state. In addition, these high

density systems show a less good fit with an exponential decay in their size distribution, there is a "hump" above the fitting line for chain lengths ~ 10 , indicating some excess of shorter chains, also suggesting that they did not reach an isotropic equilibrium state.

Like the experiments, the simulations show formation of nematic islands, oriented in random directions, growing until they reach each other, see Fig 5b. In order to facilitate the formation of longer chains in the high-density systems, global nematic order has to be established. For that to happen, the systems either need to break and reform bonds, or chains need to be able to diffuse. However, the former is inhibited by the low bond-breaking probability, while the latter is inhibited by crowding. The nematic ratio (fraction of the total number of bonds with nematic order parameter $S > 0.4$) is shown as a function of ΔT and density in Figs. 5c and d, respectively. It increases strongly with both particle density and patch-patch attraction (decreasing ΔT). To distinguish the isotropic from nematic phase, we define a threshold value of $S_{frac} = 0.3$ which corresponds to a steep increase of the nematic ratio (dashed horizontal lines in Figs. 5c and d). For systems below this line, we observe equilibrium-like polymerization with the expected monotonic dependence of chain length on particle concentration. For systems above this line, we observe signatures of kinetic arrest. The interpolated crossing

points of the $S_{frac} = 0.3$ lines with the data are used to delineate the nematic region in the tentative phase diagram Fig. 3h of the main text. Good agreement with the experimental state points is observed.

-
- [1] Zhe Gong, Theodore Hueckel, Gi Ra Yi, and Stefano Sacanna. Patchy particles made by colloidal fusion. *Nature*, 550(7675):234–238, 2017. ISSN 14764687. URL <https://www.nature.com/articles/nature23901>.
 - [2] T. F. Mohry, A. Maciolek, and S. Dietrich. Phase behavior of colloidal suspensions with critical solvents in terms of effective interactions. *J. Chem. Phys.*, 136(22):224902, 2012. doi:10.1063/1.4722883. URL <https://doi.org/10.1063/1.4722883>.
 - [3] Arnold Stein, Steven J. Davidson, Joseph C. Allegra, and Guy F. Allen. Tracer diffusion and shear viscosity for the system 2,6-lutidine-water near the lower critical point. *J. Chem. Phys.*, 56(12):6164–6168, 1972. doi:10.1063/1.1677168. URL <https://doi.org/10.1063/1.1677168>.
 - [4] H. J. Jonas, S. G. Stuij, P. Schall, and P. G. Bolhuis. A temperature-dependent critical casimir patchy particle model benchmarked onto experiment. *The Journal of Chemical Physics*, 2021. doi:10.1063/5.0055012.
 - [5] S. G. Stuij, M. Labbé-Laurent, T. Kodger, A. Maciolek, and P. Schall. Critical casimir interactions between colloids around the critical point of binary solvents. *Soft Matter*, 13. URL <http://dx.doi.org/10.1039/C7SM00599G>. 5233-5249 (2017), Chapter 3.